

Cosmo3DFlow: Wavelet Flow Matching for Spatial-to-Spectral Compression in Reconstructing the Early Universe

Md. Khairul Islam
mi3se@virginia.edu
University of Virginia
Charlottesville, Virginia, USA

Jialu Wang
walter.wang@utexas.edu
University of Texas at Austin
Austin, Texas, USA

Zeyu Xia
zeyu.xia@virginia.edu
University of Virginia
Charlottesville, Virginia, USA

Arya Farahi
arya.farahi@austin.utexas.edu
University of Texas at Austin
Austin, Texas, USA

Ryan Goudjil
kqs9vd@virginia.edu
University of Virginia
Charlottesville, Virginia, USA

Judy Fox
ckw9mp@virginia.edu
University of Virginia
Charlottesville, Virginia, USA

Abstract

Reconstructing the early Universe from the evolved present-day Universe is a challenging and computationally demanding problem in modern astrophysics. We devise a novel generative framework, Cosmo3DFlow, designed to address dimensionality and sparsity, the critical bottlenecks inherent in current state-of-the-art methods for cosmological inference. By integrating 3D Discrete Wavelet Transform (DWT) with flow matching, we effectively represent high-dimensional cosmological structures. The Wavelet Transform addresses the “void problem” by translating spatial emptiness into spectral sparsity. It decouples high-frequency details from low-frequency structures through spatial compression, and wavelet-space velocity fields facilitate stable ordinary differential equation (ODE) solvers with large step sizes. Using large-scale cosmological N -body simulations, at 128^3 resolution, we achieve up to $50\times$ faster sampling than diffusion models, combining a $10\times$ reduction in integration steps with lower per-step computational cost from wavelet compression. Our results enable initial conditions to be sampled in seconds, compared to minutes for previous methods.

CCS Concepts

- Computing methodologies → Neural networks; Unsupervised learning; Artificial intelligence; Scientific visualization;
- Applied computing → Astronomy.

Keywords

Generative models, Wavelet representation, Spatial sparsity, Spectral compression, Flow Matching, Astronomy

ACM Reference Format:

Md. Khairul Islam, Zeyu Xia, Ryan Goudjil, Jialu Wang, Arya Farahi, and Judy Fox. 2026. Cosmo3DFlow: Wavelet Flow Matching for Spatial-to-Spectral Compression in Reconstructing the Early Universe. In *Proceedings of ACM*

Permission to make digital or hard copies of all or part of this work for personal or classroom use is granted without fee provided that copies are not made or distributed for profit or commercial advantage and that copies bear this notice and the full citation on the first page. Copyrights for components of this work owned by others than the author(s) must be honored. Abstracting with credit is permitted. To copy otherwise, or republish, to post on servers or to redistribute to lists, requires prior specific permission and/or a fee. Request permissions from permissions@acm.org.

KDD '26, Jeju, Republic of Korea

© 2026 Copyright held by the owner/author(s). Publication rights licensed to ACM. ACM ISBN 978-1-4503-XXXX-X/26/06
<https://doi.org/XXXXXX.XXXXXX>

SIGKDD Conference on Knowledge Discovery and Data Mining (KDD '26).
ACM, New York, NY, USA, 11 pages. <https://doi.org/XXXXXX.XXXXXX>

1 Introduction

Understanding the origins of the universe relies on mapping the complex, non-linear structures observed today back to their initial conditions [6]. This is a *high-dimensional inverse problem* of staggering complexity, often described as trying to un-mix a fluid to determine its initial state. In the context of cosmology, the “fluid” is the distribution of dark matter and baryonic matter forms galaxies, stars, and gas. The “mixing” is driven by gravitational instability as the universe evolves.

The Sparsity Dualism: Spatial Voids vs. Spectral Compression

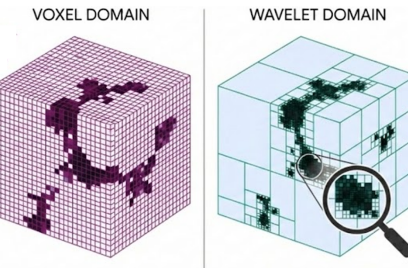


Figure 1: Schematic comparison of data representations for the Cosmic Web. Left: The voxel grid allocates memory uniformly, forcing high-resolution processing on empty void regions. **Right:** The wavelet representation adapts to structure; voids are represented by a few coarse coefficients (large blocks), while computational density is concentrated solely on the filaments and halos (dense nodes).

Analysis of N -body simulations indicates a stark disconnect between the volume a structure occupies and the mass it contains. Voids are the dominant topological feature by volume [14]. Data derived from dark matter simulations indicates that voids occupy approximately 63.7% of the total volume [14]. However, despite this volumetric dominance, they effectively represent “empty” computational space, containing only 16.2% of the dark matter mass. In contrast, filaments and halos—the regions of primary astrophysical interest where galaxies form—are sparse but mass-dense. Filaments

occupy roughly 4.3% of the volume but house 33.0% of the mass, while halos are even more extreme, representing a tiny volumetric fraction yet containing significant mass concentrations.

The cosmology inference challenge is formidable. For a simulation on a 128^3 grid (approx. 2.1 million voxels), a 64% void fraction implies that over 1.3 million voxels are dedicated to describing regions where the density contrast is low, and the gradient is near zero. A typical full N -body simulation (forward model) mapping initial conditions to observations requires numerically simulating gravitational dynamics via N -body methods, where traditional Markov Chain Monte Carlo (MCMC) approaches require thousands of forward simulations per sample. In standard Convolutional Neural Networks (CNNs) or diffusion models operating in voxel space, every one of these 1.3 million void voxels requires the same number of floating-point operations (FLOPs) as the dense, complex voxels inside a galaxy halo. This is the “uniform computation cost” mismatch of the voxel grid: resources are allocated based on volume, not information density. The voxel representation forces a “worst-case scenario” resolution across the entire domain as the solver must be fine enough everywhere to handle the densest regions, leading to massive redundancy in the sparse regions (see Figure 1 Left). This mismatch between the uniform sampling of the Eulerian grid and the heterogeneous clustering of matter is the fundamental physical driver for adopting multi-scale representations like hierarchical ball trees [30], and 3D point clouds [2] as well as wavelets.

Recent advances have opened directions for such high-dimensional problems. Legin et al. [10] showed that score-based diffusion models can successfully sample from the posterior distribution of initial density fields; however is still computationally expensive. Two recent developments in generative modeling suggest potential improvements: (1) **Flow matching** formulates generation as solving a deterministic ordinary differential equation rather than a stochastic process, typically enabling faster and more stable sampling with fewer integration steps [9]. (2) **Wavelet-based diffusion** models have demonstrated that operating in the wavelet coefficient domain rather than pixel space can provide substantial computational savings while preserving the high-frequency details crucial for many applications [4, 13]. We hypothesize that combining these two innovations is particularly well-suited for cosmological inference due to the hierarchical nature of structure formation [29].

In this work, we introduce **Cosmo3DFlow**, a framework combining flow matching with wavelet-space modeling for high-dimensional inverse problems (Figure 2). Cosmo3DFlow achieves order of magnitude speedups over diffusion baselines while matching or improving reconstruction quality. **Our main contributions are:**

- We combine **3D Discrete Wavelet Transform with flow matching for cosmological inverse problems**. The $8\times$ spatial compression from DWT serves as the key representational innovation, which enables $2\times$ larger training batches and $5\times$ lower per-step inference cost. While the total number of coefficients in a standard DWT equals the number of input pixels (preserving dimensionality in a strict mathematical sense), the effective dimensionality is drastically reduced. The “active” information—the signal variance that the model must learn—is concentrated into the coarse LLL band (which

is $1/8$ th the volume of the original grid) and a sparse subset of detail coefficients.

- We introduce wavelet-aware scale-specific conditioning that exploits the multi-resolution structure of DWT coefficients, and power spectrum regularization that enforces physically consistent density statistics during training.
- On **Quijote** 128^3 simulations, Cosmo3DFlow achieves $50\times$ faster sampling than diffusion models ($10\times$ fewer steps with $5\times$ per-step speedup) while matching or improving reconstruction fidelity (lower VRMSE, higher correlation, accurate power spectrum recovery).

2 Related Works

2.1 The Cosmological Inference Challenge

The standard model of cosmology (Λ CDM) posits that the cosmic web evolved from initial Gaussian Random Field fluctuations [3]. Gravity drives non-linear evolution, creating halos and voids [1]. Reconstructing the initial density field, denoted as y , from the evolved observation x , can be framed as a Bayesian inference task. We sample from the posterior distribution $p(y|x) = p(x|y)p(y)/p(x)$. Here, the likelihood $p(x|y)$ encapsulates the forward model of gravitational evolution (typically an N -body simulation), and the prior $p(y)$ is the Gaussian prior of the initial conditions.

The challenge is twofold: **Dimensionality**: A typical full N -body simulation volume resolved on a 128^3 grid involves over 2 million parameters (voxels). As resolutions increase, the dimensionality explodes. **Computational Cost**: Traditional statistical approaches like Bayesian Origin Reconstruction from Galaxies (BORG) [7, 8] utilize Hamiltonian Monte Carlo (HMC) to explore this high-dimensional landscape. However, this involves running the expensive forward simulation and can take thousands of CPU hours.

2.2 The Generative AI Paradigm Shift

Recent advances in deep generative modeling offer a transformative alternative: training a neural network to approximate the posterior directly. Modi et al. [16] predicted point estimates of initial conditions, Shallue and Eisenstein [22] explored invertible networks for deterministic reconstruction, and Riveros et al. [19] applied diffusion to generate 3D density fields of modified $f(R)$ gravity. Legin et al. [10] applied score-based diffusion [5, 24] to cosmological initial conditions inference, though SDE sampling in high-dimensional pixel space incurs substantial cost. Latent Diffusion Models have also been used for spatiotemporal physics emulations [20] and simulation super-resolution [15].

2.3 Flow Matching

Flow matching learns velocity fields via simple regression, offering more stable training and deterministic ODE sampling with fewer integration steps than stochastic SDEs [11]. CosmoFlow [9] demonstrated flow matching for cosmological representation learning but operated at lower resolution (2D, 256×256) without sampling full 3D volumes. FlowLensing [21] applies flow matching to 2D gravitational lensing but operates in pixel space without addressing 3D volumetric inverse problems.

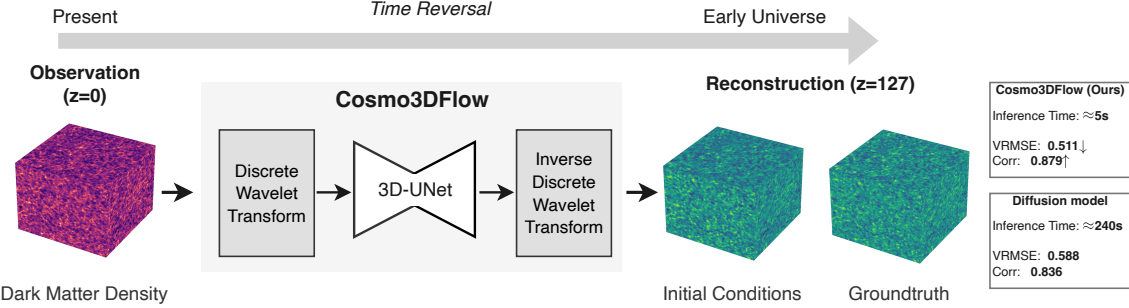


Figure 2: Cosmo3DFlow targets a high-dimensional inverse problem, while achieving 50× faster sampling. Given observations, it reconstructs samples in 5 seconds vs. ≈240 seconds for diffusion models, while preserving fine-scale structure through wavelet sparsity. Based on variance-normalized root mean squared error (VRMSE) and correlation metrics, Cosmo3DFlow demonstrates superior performance compared to diffusion.

2.4 Wavelet-Based Generative Models

Recent work [4, 18, 23] demonstrated that diffusion models in wavelet space enable efficient high-resolution generation. Phung et al. [18] showed that wavelet diffusion models can match or exceed the quality of latent diffusion models while avoiding the need to train auxiliary autoencoders. Friedrich et al. [4] adapted discrete wavelet diffusion for high-resolution 3D medical imaging. Mebratu and Wu [13] used Wavelet Flow to model the field-level probability distributions of extragalactic foregrounds in cosmic microwave background (CMB) observations. Georgios et al. [26] applied Wavelet Scattering Transform to constrain the nature of gravity using 3D N-body simulations.

3 Methodology

3.1 Problem Formulation

High-dimensional cosmological inference is challenging due to the sparsity of the data distribution (space is mostly empty) and the significant computational requirements. We formalize our goal as a conditional generation problem: given an observation $y \in \mathbb{R}^{N^3}$ (evolved state), sample from the posterior $p(x|y)$ over latent states $x \in \mathbb{R}^{N^3}$ (initial conditions). With $N = 128$, this involves ~ 2 million dimensions. The forward process $y = f(x)$ is nonlinear and expensive to evaluate (requiring numerical simulation), making traditional MCMC intractable. Our goal is to train a generative model that produces diverse, high-quality samples conditioned on y .

3.2 Flow Matching Framework

Flow matching learns continuous normalizing flows by regressing velocity fields that transport samples from a simple prior p_0 to the target data distribution p_1 [11]. Given samples from the prior $x_0 \sim p_0$ and target $x_1 \sim p_1$, we define an interpolation path:

$$x_t = \mu_t(x_0, x_1) = t x_1 + (1 - t) x_0, \quad t \in [0, 1] \quad (1)$$

This linear interpolation, known as rectified flow [12], yields a constant target velocity field:

$$u_t = \frac{dx_t}{dt} = x_1 - x_0 \quad (2)$$

For conditional generation with observation y , we train a velocity network $v_\theta(x_t, t, y)$ to approximate this target velocity by minimizing the flow matching objective:

$$\mathcal{L}_{FM} = \mathbb{E}_{t \sim \mathcal{U}(0,1), x_0 \sim p_0, x_1 \sim p_1} [\|v_\theta(x_t, t, y) - u_t\|^2] \quad (3)$$

At inference time, we sample initial noise $x_0 \sim \mathcal{N}(0, I)$ and integrate the learned velocity field to obtain the final sample:

$$x_1 = x_0 + \int_0^1 v_\theta(x_t, t, y) dt \quad (4)$$

where the integral accumulates the velocity contributions along the flow trajectory, transporting the initial noise x_0 to the target distribution. In practice, we approximate this integral using a numerical ODE solver with K discrete steps. The deterministic nature of ODE integration, as opposed to SDEs in diffusion models, enables more stable and efficient generation.

3.3 Wavelet Flow Matching

3.3.1 Wavelet Domain Transformation. The Discrete Wavelet Transform (DWT) consists of separable convolutions with low-pass (L) and high-pass (H) filters followed by downsampling by a factor of 2 along each spatial dimension. For a 3D volume $y \in \mathbb{R}^{D \times H \times W}$, this decomposition yields eight wavelet coefficient tensors:

$$(c_{LLL}, c_{LLH}, c_{LHL}, c_{LHH}, c_{HLL}, c_{HLH}, c_{HHL}, c_{HHH}) = DWT(y) \quad (5)$$

where each coefficient tensor has dimensions $c_* \in \mathbb{R}^{D/2 \times H/2 \times W/2}$. We use the Haar wavelet basis, which applies box-averaging for the low-pass filter and pairwise differencing for the high-pass filter along each axis, providing perfect reconstruction and computational efficiency through simple addition and subtraction operations.

The approximation coefficient c_{LLL} captures low-frequency content representing large-scale structure, while the remaining seven detail coefficients encode high-frequency information along different directional orientations. We stack these coefficients along the channel dimension to form a unified representation:

$$\tilde{y} = \text{Stack}(c_{LLL}/\sqrt{8}, c_{LLH}, \dots, c_{HHH}) \in \mathbb{R}^{8 \times D/2 \times H/2 \times W/2} \quad (6)$$

Algorithm 1 Cosmo3DFlow Training

Require: Dataset $\mathcal{D} = \{(\mathbf{x}_i, \mathbf{y}_i)\}_{i=1}^N$, velocity model v_θ , wavelet mixer m_ϕ
Require: Hyperparameters: λ_{PS} (power spectrum weight), T_{prog} (epochs per level)
Ensure: Trained parameters θ^*, ϕ^*

- 1: Initialize v_θ, m_ϕ , Exponential Moving Average (EMA) with decay 0.99
- 2: Set wavelet level $L \leftarrow 1$
- 3: **for** epoch $e = 1, \dots, E_{\max}$ **do**
- 4: **for** each batch (\mathbf{x}, \mathbf{y}) **do**
- 5: Sample $t \sim \mathcal{U}(0, 1)$, $\mathbf{x}_0 \sim \mathcal{N}(\mathbf{0}, \mathbf{I})$
// Conversion to wavelet domain
- 6: $\mathbf{w}_0 \leftarrow \text{DWT}(\mathbf{x}_0)$, $\mathbf{w}_1 \leftarrow \text{DWT}(\mathbf{x})$, $\tilde{\mathbf{y}} \leftarrow \text{DWT}(\mathbf{y})$
- 7: $\mathbf{w}_t \leftarrow t\mathbf{w}_1 + (1-t)\mathbf{w}_0$
- 8: **UNet Forward Pass with Scale Conditioning and Cross-Scale Skips (Algorithm 3)**
- 9: $\mathbf{v}_t \leftarrow v_\theta(\mathbf{w}_t, t, \tilde{\mathbf{y}})$
- 10: $\mathcal{L}_{FM} \leftarrow \|\mathbf{v}_t - (\mathbf{w}_1 - \mathbf{w}_0)\|^2$ // flow matching loss
- 11: **Physics Loss Regularization**
- 12: $P_{pred} \leftarrow \text{PowerSpec}(\text{IDWT}(\mathbf{M} \odot \mathbf{v}_t))$
- 13: $P_{true} \leftarrow \text{PowerSpec}(\text{IDWT}(\mathbf{M} \odot (\mathbf{w}_1 - \mathbf{w}_0)))$
- 14: $\mathcal{L}_{PS} \leftarrow \|\log P_{pred} - \log P_{true}\|^2$
- 15: $\mathcal{L} \leftarrow \mathcal{L}_{FM} + \lambda_{PS} \mathcal{L}_{PS}$
- 16: Update θ, ϕ via gradient descent
- 17: Update EMA parameters
- 18: **end for**
- 19: **end for**
- 20: **return** EMA-averaged θ^*, ϕ^*

Algorithm 2 Inference: Sample Initial Conditions

Require: Observed \mathbf{y} , trained model v_{θ^*} , ODE steps N
Ensure: Initial condition $\hat{\mathbf{x}}$

- 1: $\tilde{\mathbf{y}} \leftarrow \text{DWT}(\mathbf{y})$
- 2: Sample $\mathbf{w}_0 \sim \mathcal{N}(\mathbf{0}, \mathbf{I})$
- 3: **for** $n = 1$ to N **do**
- 4: $t \leftarrow n/N$
- 5: $\mathbf{v} \leftarrow v_{\theta^*}(\mathbf{w}_{n-1}, t, \tilde{\mathbf{y}})$ // Use EMA model
- 6: $\mathbf{w}_n \leftarrow \mathbf{w}_{n-1} + (1/N)\mathbf{v}$
- 7: **end for**
- 8: $\hat{\mathbf{x}} \leftarrow \text{IDWT}(\mathbf{w}_N)$
- 9: **return** $\hat{\mathbf{x}}$

where we normalize \mathbf{c}_{LLL} by $\sqrt{8}$ to balance the energy distribution across coefficients. The original field can be exactly recovered via the Inverse Discrete Wavelet Transform (IDWT): $\mathbf{y} = \text{IDWT}(\tilde{\mathbf{y}})$.

The wavelet representation offers three key advantages for cosmological inference:

- (1) **Sparse representations:** Wavelet coefficients of cosmological density fields exhibit sparse, structured distributions that are more amenable to generative modeling than dense voxel representations.
- (2) **Spatial compression:** An eight-fold reduction in spatial dimensions from N^3 to $8 \times (N/2)^3$ voxels while preserving

complete information, reducing memory requirements and computational cost.

- (3) **Physical alignment:** The multi-resolution decomposition mirrors the hierarchical nature of cosmological structure formation, where large-scale density fluctuations are established early during inflation and small-scale structures develop through subsequent gravitational collapse.

3.3.2 Wavelet-Space Flow Matching. We formulate the flow matching objective entirely in wavelet space. Let $\tilde{\mathbf{x}}_0 = \text{DWT}(\mathbf{x}_0)$ and $\tilde{\mathbf{x}}_1 = \text{DWT}(\mathbf{x}_1)$ denote the wavelet-transformed noise and target fields, respectively. The wavelet-space loss becomes:

$$\mathcal{L}_{\text{flow}} = \mathbb{E}_{t, \tilde{\mathbf{x}}_0, \tilde{\mathbf{x}}_1} [\|\mathbf{v}_\theta(\tilde{\mathbf{x}}_t, t, \tilde{\mathbf{y}}) - (\tilde{\mathbf{x}}_1 - \tilde{\mathbf{x}}_0)\|^2] \quad (7)$$

where $\tilde{\mathbf{x}}_t = t\tilde{\mathbf{x}}_1 + (1-t)\tilde{\mathbf{x}}_0$ is the interpolated state in wavelet space, and $\tilde{\mathbf{y}} = \text{DWT}(\mathbf{y})$ is the wavelet-transformed conditioning observation.

At inference time, we sample initial Gaussian noise $\mathbf{x}_0 \sim \mathcal{N}(\mathbf{0}, \mathbf{I})$ in voxel space, transform to wavelet domain $\tilde{\mathbf{x}}_0 = \text{DWT}(\mathbf{x}_0)$, integrate the velocity field in wavelet space, and apply the inverse wavelet transform to recover the final density field:

$$\hat{\mathbf{x}}_1 = \text{IDWT} \left(\tilde{\mathbf{x}}_0 + \int_0^1 \mathbf{v}_\theta(\tilde{\mathbf{x}}_t, t, \tilde{\mathbf{y}}) dt \right) \quad (8)$$

Here, $\tilde{\mathbf{x}}_0$ represents the initial state (transformed noise) and the integral accumulates the velocity field contributions that transport this initial state toward the target distribution conditioned on $\tilde{\mathbf{y}}$. In practice, we approximate this integral using a numerical ODE solver (e.g., Euler or higher-order Runge-Kutta methods) with K discrete steps.

3.3.3 Power Spectrum Regularization. To ensure that generated fields respect the statistical properties of cosmological density fields, we optionally incorporate a power spectrum loss. Since the initial conditions are a Gaussian random field, the power spectrum serves as a sufficient statistic, making this a physically motivated and powerful form of regularization. The 3D isotropic power spectrum $P(k)$ characterizes the variance of density fluctuations as a function of wavenumber $k = |\mathbf{k}|$. We compute the power spectrum via the discrete Fourier transform and radial binning:

$$P(k_i) = \frac{1}{N_{\text{modes}}(k_i)} \sum_{|\mathbf{k}| \in \text{bin}_i} |\tilde{\delta}(\mathbf{k})|^2 \quad (9)$$

where $\tilde{\delta}(\mathbf{k})$ denotes the Fourier transform of the density contrast field and $N_{\text{modes}}(k_i)$ counts modes in the i -th radial bin.

The power spectrum loss penalizes discrepancies in log-space to treat relative errors uniformly across the dynamic range:

$$\mathcal{L}_{PS} = \sum_{i=1}^{N_{\text{bins}}} (\log P_{\text{pred}}(k_i) - \log P_{\text{target}}(k_i))^2 \quad (10)$$

This regularization is applied to the predicted and target velocities after they are transformed back to voxel space via the inverse DWT. The combined training objective becomes:

$$\mathcal{L}_{\text{total}} = \mathcal{L}_{\text{flow}} + \lambda_{PS} \mathcal{L}_{PS} \quad (11)$$

where λ_{PS} is a hyperparameter controlling the strength of the power spectrum regularization. We keep the value at 0.01.

3.4 Network Architecture

3.4.1 3D U-Net Velocity Network. Our velocity network v_θ follows a 3D U-Net architecture adapted for volumetric cosmological data. The network takes as input the concatenation of the noisy wavelet coefficients $\tilde{\mathbf{x}}_t \in \mathbb{R}^{8 \times D/2 \times H/2 \times W/2}$ and the conditioning observation $\tilde{\mathbf{y}} \in \mathbb{R}^{8 \times D/2 \times H/2 \times W/2}$, yielding 16 input channels. The output has 8 channels corresponding to the predicted velocity in wavelet space.

Time Embedding. The continuous time variable $t \in [0, 1]$ is embedded using Gaussian Fourier features [25]:

$$\gamma(t) = [\sin(2\pi \mathbf{W}t), \cos(2\pi \mathbf{W}t)] \in \mathbb{R}^{2d} \quad (12)$$

where $\mathbf{W} \in \mathbb{R}^d$ are learnable frequency parameters initialized from $\mathcal{N}(0, \sigma^2)$ with $\sigma = 16$. This embedding is projected through two linear layers with Sigmoid Linear Unit (SiLU) activations to produce the time embedding $\mathbf{e}_t \in \mathbb{R}^{4n_f}$, where $n_f = 32$ is the base feature dimension.

Encoder Path. The encoder downsamples the input volume to a fixed spatial dimension of $8 \times 8 \times 8$. Thus, 32^3 , 64^3 , and 128^3 resolutions are downsampled 2, 3, and 4 times, respectively. Each resolution level contains $N_{\text{res}} = 2$ residual blocks followed by spatial downsampling. The residual blocks employ the BigGAN-style architecture:

$$\mathbf{h}' = \text{Conv}(\text{SiLU}(\text{GN}(\mathbf{h}))) + \text{Dense}(\text{SiLU}(\mathbf{e}_t)) \quad (13)$$

$$\mathbf{h}'' = \text{Conv}(\text{Dropout}(\text{SiLU}(\text{GN}(\mathbf{h}')))) \quad (14)$$

$$\text{ResBlock}(\mathbf{h}, \mathbf{e}_t) = (\mathbf{h}'' + \text{Skip}(\mathbf{h}))/\sqrt{2} \quad (15)$$

where GN denotes Group Normalization (GN) with $\min(c/4, 32)$ groups (where c is the number of channels), and Skip denotes a 1×1 convolution when channel dimensions change. Downsampling is performed via strided average pooling.

Decoder Path. The decoder mirrors the encoder structure with skip connections from corresponding encoder levels. At each resolution, features from the skip connection are concatenated with upsampled features before passing through residual blocks. Upsampling is performed via nearest-neighbor interpolation followed by convolution.

Output Layer. The final output is produced by Group Normalization, SiLU activation, and a $3 \times 3 \times 3$ convolution projecting to 8 output channels.

3.4.2 Wavelet-Aware Architectural Enhancements. We introduce three optional architectural modifications designed to exploit the structure of wavelet representations:

Scale-Specific Conditioning. Rather than treating all wavelet bands uniformly, we inject scale-specific information at each resolution level of the U-Net. At resolution level i , we project the 8-channel wavelet observation through a $1 \times 1 \times 1$ convolution:

$$\mathbf{z}_i = \text{Conv}_{1 \times 1 \times 1}(\tilde{\mathbf{y}}) \in \mathbb{R}^{n_f \cdot m_i \times D_i \times H_i \times W_i} \quad (16)$$

followed by adaptive average pooling to match the spatial dimensions. This conditioning is added to the hidden state after each residual block, providing direct access to scale-relevant information at each resolution.

Cross-Scale Skip Connections. To facilitate information flow between different wavelet scales during generation, we introduce additional skip connections that bridge encoder features directly to corresponding decoder levels through learned $1 \times 1 \times 1$ projections:

$$\mathbf{h}_{\text{dec}}^{(i)} = \mathbf{h}_{\text{dec}}^{(i)} + \text{Conv}_{1 \times 1 \times 1}(\mathbf{h}_{\text{enc}}^{(i)}) \quad (17)$$

These connections allow the model to maintain coherent scale relationships throughout the generation process.

3.5 Training and Inference

We summarize the training procedure in Algorithm 1 and the inference procedure in Algorithm 2.

Training. We use AdamW optimization with learning rate $\eta = 10^{-4}$ and a ReduceLROnPlateau scheduler with patience 5 and factor 0.5. Gradient clipping with maximum norm 1.0 ensures stable training. Data augmentation via random 3D rotations and reflections improves generalization. Each model is trained for 100 epochs, and the best model by validation loss is selected for testing. We used batch sizes 16, 8, and 4 for the 32^3 , 64^3 , and 128^3 resolutions, respectively. All training and inference use the NVIDIA A100 GPU with 80 GB of memory.

Inference. At test time, we sample Gaussian noise in voxel space, transform to wavelet domain, and integrate the learned velocity field using the Euler method with K steps:

$$\tilde{\mathbf{x}}_{(k+1)/K} = \tilde{\mathbf{x}}_{k/K} + \frac{1}{K} \mathbf{v}_\theta \left(\tilde{\mathbf{x}}_{k/K}, \frac{k}{K}, \tilde{\mathbf{y}} \right) \quad (18)$$

for $k = 0, 1, \dots, K-1$. The final output is recovered via the IDWT: $\hat{\mathbf{x}} = \text{IDWT}(\tilde{\mathbf{x}}_1)$. The wavelet-space formulation enables accurate sampling with much fewer steps compared to the diffusion-based approaches.

4 Experiment

4.1 Experimental Settings

Dataset	#Samples	Parameters Varied	Strategy	Description
Standard LH	2,000	$\Omega_m, \Omega_b, h, n_s, \sigma_8$	Latin-Hypercube	Baseline Λ CDM suite
Big Sobol (BSQ)	1,000	$\Omega_m, \Omega_b, h, n_s, \sigma_8$	Sobol Sequence	Collection of simulations
fNL_LH (Local)	1,000	$f_{NL}^{\text{local}} \in [-300, 300]$	Latin-Hypercube	Primordial non-Gaussianity

Table 1: Selected Quijote simulation datasets.

4.1.1 Dataset. We evaluate on the following datasets from the **Quijote Latin Hypercube simulations** [28]¹, summarized in Table 1. All suites use a periodic box volume of $(1000 h^{-1}\text{Mpc})^3$ with 512^3 particles. For the Standard LH and BSQ sets, the five core

¹<https://quiijote-simulations.readthedocs.io/en/latest/LH.html>

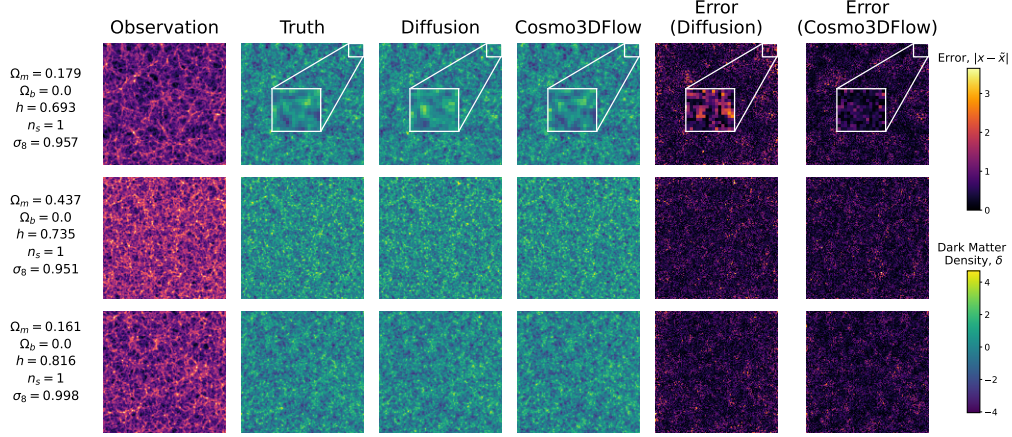


Figure 3: Qualitative comparison of reconstruction quality. 2D slices through 3D density fields at $z = 127$ for three test samples from the Standard Latin Hypercube. Columns show: observation y at $z = 0$, ground truth initial conditions x , Diffusion, and Cosmo3DFlow (ours) reconstruction, and absolute error maps. Dashed boxes highlight small-scale structure differences—the baseline exhibits smoothing artifacts (blurry), while Cosmo3DFlow preserves sharp features. Error maps demonstrate that Cosmo3DFlow achieves consistently lower reconstruction error across all samples, particularly in high-density regions. Colorbars indicate dark matter density contrast δ and absolute error magnitude.

Λ CDM parameters are varied. In the f_{NL} Local set, these parameters are held fixed at the fiducial cosmology ($\Omega_m = 0.3175$, $\Omega_b = 0.049$, $h = 0.6711$, $n_s = 0.9624$, $\sigma_8 = 0.834$) to isolate the impact of primordial non-Gaussianity on large-scale structure. We collect the snapshots from the publicly available source at redshifts $z = 127$ (initial conditions) and $z = 0$ (present-day universe).

Standard Latin Hypercube (LH): This suite comprises 2000 full N -body dark matter simulations with cosmological parameters sampled uniformly across $\Omega_m \in [0.1, 0.5]$, $\Omega_b \in [0.03, 0.07]$, $\sigma_8 \in [0.6, 1.0]$, $h \in [0.5, 0.9]$, and $n_s \in [0.8, 1.2]$. We partition the simulations into training, validation, and test sets of sizes 1800, 100, and 100, respectively.

Big Sobol Sequence (BSQ): A large collection of N -body simulations designed for machine learning. We use the first 1000 samples, split 8:1:1 for train, validation, and test.

Non-Gaussian Local Latin Hypercube (LH): 1,000 simulations exploring the impact of primordial non-Gaussianities on large-scale structure, split 8:1:1.

Density Field Construction: The 3D matter density fields were constructed from the N -body simulation snapshots using the Pylians library [27] following [10]. For the late-time snapshots at $z = 0$, we employed the Piecewise Cubic Spline (PCS) mass assignment scheme to minimize aliasing and ensure a high-fidelity representation of the non-linear cosmic web. For the initial conditions at $z = 127$, we utilized the Cloud-in-Cell (CIC) scheme, which is sufficient for the low-contrast fluctuations at high redshift. Each density field was computed at three resolutions (32^3 , 64^3 , and 128^3) and converted into the dimensionless overdensity field, $\delta(\mathbf{x}) = \rho(\mathbf{x})/\bar{\rho} - 1$, to serve as the input and target for our generative models. We apply a logarithmic transformation to the $z = 0$ observation fields due to their high dynamic range. Both fields are standardized afterwards for model training.

4.1.2 Evaluation Metrics. We consider several metrics for evaluation, each serving a different purpose. All are implemented using the Pylians library [27].

Variance-normalized root mean squared error (VRMSE): The root mean squared error (RMSE) and its normalized variants are widespread metrics to quantify the point-wise accuracy of simulations [17, 20]. Formally, for two spatial fields \mathbf{u} and \mathbf{v} , the VRMSE is defined as follows, where $\langle \cdot \rangle$ denotes the spatial mean operator, and $\epsilon = 10^{-6}$ is a numerical stability term:

$$\text{VRMSE}(\mathbf{u}, \mathbf{v}) = \sqrt{\frac{\langle (\mathbf{u} - \mathbf{v})^2 \rangle}{\langle (\mathbf{u} - \langle \mathbf{u} \rangle)^2 \rangle + \epsilon}} \quad (19)$$

Power Spectrum R^2 -score: The predicted dark matter density distribution should stay similar to the ground truth. Following [19], we calculate the R^2 -score of the target 3D density field and the predicted samples. This shows how the model performs over the power spectrum.

Cross-Correlation, $C(k)$: This quantifies the scale-dependent loss between reconstructed and true density fields, providing a measure insensitive to overall amplitude normalization [8, 16]. It is computed using the following, where $P_{11}(k)$ and $P_{22}(k)$ denote the power spectra of the sample and truth, respectively:

$$C(k) = \frac{P_{12}(k)}{\sqrt{P_{11}(k) \cdot P_{22}(k)}} \quad (20)$$

Transfer Function, $T(k)$: The transfer function $T(k)$ characterizes the scale-dependent fidelity of reconstruction by measuring the ratio of recovered to true power at each spatial scale. We define the transfer function as:

$$T(k) = \sqrt{\frac{P_{\text{sample}}(k)}{P_{\text{true}}(k)}} \quad (21)$$

Dataset	Resolution	VRMSE ↓		Cross Correlation ↑		Power Spectrum R^2 -score ↑		Transfer Function ↑	
		Ours	Diffusion	Ours	Diffusion	Ours	Diffusion	Ours	Diffusion
Standard	128^3	0.50	0.63	0.88	0.82	0.99	0.70	0.99	0.80
Latin	64^3	0.47	0.68	0.92	0.89	0.98	0.59	0.98	0.59
Hypercube	32^3	0.34	0.82	0.96	0.85	0.95	0.48	0.95	0.48
Big Sobol Sequence	128^3	0.62	0.64	0.80	0.79	0.99	0.84	0.95	0.88
	64^3	0.53	0.65	0.88	0.88	0.98	0.83	0.94	0.81
	32^3	0.37	0.79	0.95	0.55	0.95	0.48	0.94	0.71
Non-Gauss (f _{NL} LH)	128^3	0.56	0.59	0.86	0.83	1.00	1.00	0.98	0.98
	64^3	0.47	0.57	0.93	0.89	1.00	1.00	0.99	0.99
	32^3	0.31	0.67	0.97	0.87	1.00	0.98	0.99	0.98

Table 2: Performance comparison on Quijote simulation datasets. The best results are in bold. Cosmo3DFlow (Ours) shows superior performance across resolutions over the baseline (diffusion).

We quantify transfer function accuracy through the mean absolute deviation from the ideal value $\epsilon_T = \frac{1}{N_k} \sum_k |T(k) - 1|$.

4.1.3 Baseline. We use the Score-based diffusion model from Legin et al. [10] as the baseline generative model, as they achieved the recent significant breakthrough on our target problem. We annotate this as the "Diffusion" baseline. The Unet model parameters are kept the same as our model to get a fixed latent dimension ($8 \times 8 \times 8$) across resolutions. So, for a resolution, the compression ratio is the same. This ensures a fair comparison between these two models.

4.2 Results

We compare Cosmo3DFlow against the diffusion baseline across multiple dimensions: convergence (Figure 5), efficiency–quality trade-off (Figure 4), physics validation metrics (Figure 6), and qualitative reconstruction fidelity (Figure 3). Quantitative results are summarized in Table 2. As shown in Table 2, Cosmo3DFlow consistently outperforms the diffusion baseline across all datasets and resolutions. At 128^3 on the Standard Latin Hypercube test set, it achieves a VRMSE of 0.50 vs. 0.63, cross-correlation of 0.88 vs. 0.82, and a power spectrum R^2 -score of 0.99 vs. 0.70. These gains are consistent across the Big Sobol Sequence and Non-Gaussian datasets, demonstrating robustness to varying cosmological parameters and primordial non-Gaussianity.

4.3 Ablation Study

We evaluate the impact of our added components on model performance at 32^3 resolution using the Standard Latin Hypercube test set. To ensure a fair comparison, the baseline (without wavelets) utilizes an additional downsampling/upsampling layer to maintain the same compression ratio (latent dimension $8 \times 8 \times 8$) as the wavelet-based configurations. Table 3 shows that the baseline flow model already achieves good performance. We omitted the cross-correlation since all models achieved a value of around 0.98 in this case. Applying the wavelet directly negatively impacts the VRMSE score. The introduction of Scale Conditioning and Cross-Scale Skips bridges the gap between spatial and wavelet domains, providing the necessary context to resolve features across different scales. The power spectrum weight ensures the generated fields adhere to physical statistics.

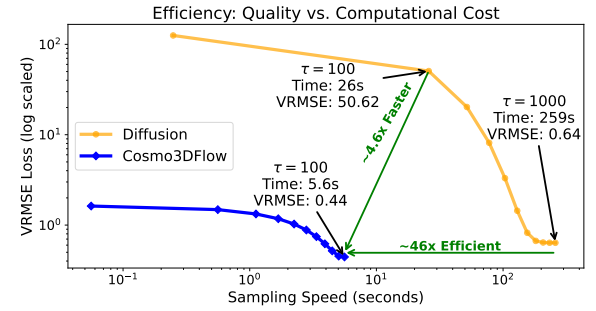


Figure 4: Computational efficiency vs. reconstruction quality: Cosmo3DFlow achieves significantly faster sampling (4.4× at the same number of steps) and maintains accuracy despite using 10× fewer steps.

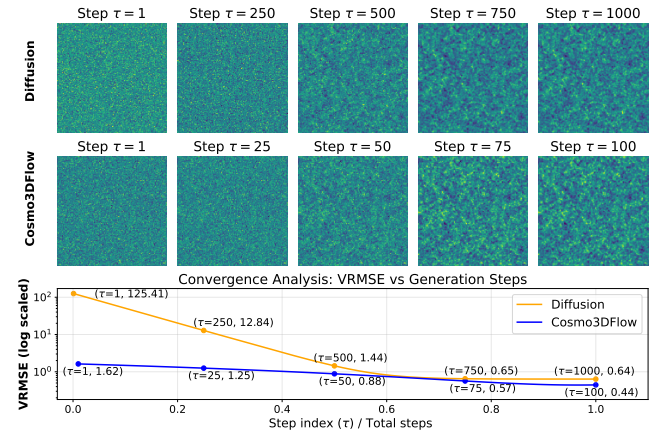


Figure 5: The generation process for a test sample. Showing how the models reconstruct the target simulation from Gaussian noise. The VRMSE loss at the last row (lower is better) shows significantly faster convergence of our proposed model.

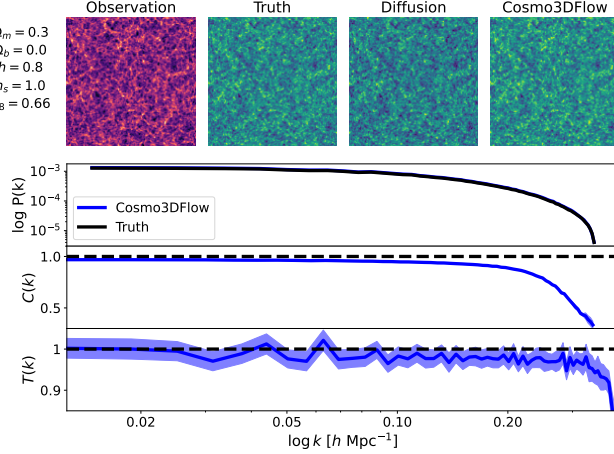


Figure 6: The top row shows an example input, observation condition, and generated output from Diffusion and our Cosmo3DFlow model. Rows 2–4 show physics validation metrics on a log-scaled x-axis. Row 2: Power spectrum $P(k)$ as a function of wavenumber k ; our prediction shows near-perfect alignment with the true distribution. Row 3: Cross-correlation $C(k)$ shows Cosmo3DFlow achieves near-perfect correlation ($C \approx 1$) across most scales. Row 4: Transfer function $T(k)$ is close to unity (dashed line), indicating accurate amplitude recovery. The shaded regions represent 95% confidence intervals around the mean.

Components				Evaluation Metrics		
Wavelet	Scale Condition	Skips	$P(k)$ Weight	VRMSE \downarrow	$R^2 \uparrow$	Transfer Function \uparrow
✗	✗	✗	✗	0.26	0.95	0.94
✓	✗	✗	✗	0.34	0.95	0.95
✓	✓	✓	✗	0.27	0.96	0.96
✓	✓	✓	0.01	0.25	0.97	0.96

Table 3: Ablation study of model components evaluated on the Standard Latin Hypercube. Showing that the added components have a positive impact on the overall performance.

The Cosmo3DFlow framework performs computations within a decomposed coefficient space rather than the high-resolution spatial domain. As shown in Table 4 and demonstrated in our ablation study, this mitigates the cubic scaling bottlenecks inherent in 128^3 volumes, achieving a 61.9% reduction in peak memory compared to standard flow matching and an 89.2% decrease relative to diffusion baselines. Beyond memory conservation, the wavelet-enabled framework exhibits superior speed; at the 128^3 scale, it maintains a throughput over $46\times$ faster than diffusion. These results indicate that wavelet decomposition effectively preserves structural fidelity while lowering the computational overhead.

Resol- ution	Metric	Diffusion	Flow Matching		Improvement vs Diffusion
			wo/ Wavelet	w/ Wavelet	
32^3	Time (s)	27.9	1.32	0.72	$38.7\times$ faster
	Memory	19.8K	383	159	99.2%
64^3	Time	221	3.51	1.23	$179.7\times$ faster
	Memory	19.8K	828	431	97.8%
128^3	Time	243	23.7	5.20	$46.8\times$ faster
	Memory	19.9K	5.6k	2.1k	89.2%

Table 4: Sampling Efficiency Comparison: Diffusion vs. Flow Matching (FM) with and without wavelet decomposition. Evaluated on a single NVIDIA A100 80GB GPU. FM uses 100 sampling steps; Diffusion uses 1000. Time and memory are reported in seconds and MB, respectively.

5 Conclusion

We introduced Cosmo3DFlow, a generative framework combining flow matching with wavelet-space modeling for high-dimensional inverse problems. By transforming density fields into the wavelet domain, topological voids collapse into near-zero high-frequency coefficients while information-rich structures are preserved compactly—a physically informed exploitation of *wavelet sparsity*. This achieves up to $50\times$ faster sampling than diffusion baselines at 128^3 resolution, as wavelet decomposition naturally aligns with multi-scale cosmological structure, enabling sparse velocity fields that require far fewer ODE integration steps.

As cosmological simulations scale to larger volumes and finer resolutions (512^3 , 1024^3), the voxel void fraction will remain constant or increase (as we resolve smaller voids), but the computational cost of processing it on a grid will scale cubically (N^3). Wavelet sparsity breaks this scaling law. It ensures that computational resources are allocated to the structure of the universe—the mass, the energy, and the information—rather than its emptiness. This shift from spatial to spectral modeling represents not just an optimization, but a necessary evolution for the next generation of high-dimensional astrophysical inference.

Limitations and Ethical Considerations

Our method focuses on dark matter-only simulations; other simulation suites and alternative wavelet families remain to be explored. The synthetic simulation data poses no privacy or ethical concerns. We will release code and model weights to ensure reproducibility.

GenAI Disclosure

Google Gemini was used for the initial drafting of figures. Claude Opus was used for text polishing.

Acknowledgement

This work is partly supported by NSF-Simons AI Institute for Cosmic Origins (CosmicAI: Grant 2421782).

References

- [1] J. M. Bardeen, J. R. Bond, N. Kaiser, and A. S. Szalay. 1986. The Statistics of Peaks of Gaussian Random Fields. *The Astrophysical Journal* 304 (May 1986), 15. doi:10.1086/164143
- [2] Atriade Chatterjee and Francisco Villaescusa-Navarro. 2025. Cosmology from Point Clouds with Dark Matter Halos from the Quijote Simulations. *The Astrophysical Journal* 985, 1 (May 2025), 132. doi:10.3847/1538-4357/adc99d
- [3] Scott Dodelson and Fabian Schmidt. 2020. *Modern Cosmology*. Academic Press, Cambridge, MA. doi:10.1016/C2017-0-01943-2
- [4] Paul Friedrich, Julia Wolleb, Florentin Bieder, Alicia Durrer, and Philippe C. Catton. 2025. WDM: 3D Wavelet Diffusion Models for High-Resolution Medical Image Synthesis. In *Deep Generative Models*, Anirban Mukhopadhyay, Ilkay Okusuz, Sandy Engelhardt, Dorit Mehrof, and Yixuan Yuan (Eds.). Springer Nature Switzerland, Cham, 11–21. doi:10.1007/978-3-031-72744-3_2
- [5] Jonathan Ho, Ajay Jain, and Pieter Abbeel. 2020. Denoising Diffusion Probabilistic Models. In *Advances in Neural Information Processing Systems*, Vol. 33. Curran Associates, Inc., Vancouver, Canada, 6840–6851.
- [6] Dragan Huterer. 2023. *A Course in Cosmology: From Theory to Practice*. Cambridge University Press, Cambridge, UK.
- [7] J. Jasche and G. Lavaux. 2019. Physical Bayesian Modelling of the Non-Linear Matter Distribution: New Insights into the Nearby Universe. *Astronomy & Astrophysics* 625 (May 2019), A64. doi:10.1051/0004-6361/201833710
- [8] Jens Jasche and Benjamin D. Wandelt. 2013. Bayesian Physical Reconstruction of Initial Conditions from Large-Scale Structure Surveys. *Monthly Notices of the Royal Astronomical Society* 432, 2 (June 2013), 894–913. doi:10.1093/mnras/stt449
- [9] Sidharth Kannan, Tian Qiu, Carolina Cuesta-Lazaro, and Haewon Jeong. 2025. CosmoFlow: Scale-Aware Representation Learning for Cosmology with Flow Matching. arXiv:2507.11842 [astro-ph]
- [10] Ronan Legin, Matthew Ho, Pablo Lemos, Laurence Perreault-Levasseur, Shirley Ho, Yashar Hezaveh, and Benjamin Wandelt. 2024. Posterior Sampling of the Initial Conditions of the Universe from Non-Linear Large Scale Structures Using Score-Based Generative Models. *Monthly Notices of the Royal Astronomical Society: Letters* 527, 1 (Jan. 2024), L173–L178. doi:10.1093/mnrasl/slad152
- [11] Yaron Lipman, Ricky T. Q. Chen, Heli Ben-Hamu, Maximilian Nickel, and Matt Le. 2023. Flow Matching for Generative Modeling. arXiv:2210.02747 [cs]
- [12] Xingchao Liu, Chengyue Gong, and Qiang Liu. 2022. Flow Straight and Fast: Learning to Generate and Transfer Data with Rectified Flow. arXiv:2209.03003 [cs]
- [13] M. Mebratu and W. L. K. Wu. 2025. Wavelet Flow For Extragalactic Foreground Simulations. arXiv:2505.21220 [astro-ph]
- [14] Ofer Metuki, Noam I. Libeskind, Yehuda Hoffman, Robert A. Crain, and Tom Theuns. 2015. Galaxy Properties and the Cosmic Web in Simulations. *Monthly Notices of the Royal Astronomical Society* 446, 2 (Jan. 2015), 1458–1468. doi:10.1093/mnras/stu2166
- [15] Satvik Mishra, Roberto Trotta, and Matteo Viel. 2026. Cosmo-FOLD: Fast Generation and Upscaling of Field-Level Cosmological Maps with Overlap Latent Diffusion. arXiv:2601.14377 [astro-ph] doi:10.48550/arXiv.2601.14377
- [16] C. Modi, F. Lanusse, and U. Seljak. 2021. FlowPM: Distributed TensorFlow Implementation of the FastPM Cosmological N-body Solver. *Astronomy and Computing* 37 (Oct. 2021), 100505. doi:10.1016/j.ascom.2021.100505
- [17] Ruben Ohana, Michael McCabe, Lucas Meyer, Rudy Morel, Fruzsina J. Agocs, Miguel Beneitez, Marsha Berger, Blakesley Burkhardt, Stuart B. Dalziel, Drummond B. Fielding, Daniel Fortunato, Jared A. Goldberg, Keiya Hirasima, Yan-Fei Jiang, Rich R. Kerswell, Suryanarayana Maddu, Jonah Miller, Payel Mukhopadhyay, Stefan S. Nixon, Jeff Shen, Romain Watteaux, Bruno R. Blanchard, Francois Rozet, Liam H. Parker, Miles Crammer, and Shirley Ho. 2024. The Well: A Large-Scale Collection of Diverse Physics Simulations for Machine Learning. *Advances in Neural Information Processing Systems* 37 (Dec. 2024), 44989–45037. doi:10.5220/079017-1430
- [18] Hao Phung, Quan Dao, and Anh Tran. 2023. Wavelet Diffusion Models Are Fast and Scalable Image Generators. In *2023 IEEE/CVF Conference on Computer Vision and Pattern Recognition (CVPR)*. IEEE, Vancouver, BC, Canada, 10199–10208. doi:10.1109/CVPR52729.2023.00983
- [19] Julieth K Riveros, Paola A Saavedra, Héctor J Hortúa, Jorge Enrique García-Farieta, and Ivan Olier. 2025. Conditional Diffusion-Flow models for generating 3D cosmic density fields: applications to f(R) cosmologies. *Machine Learning: Science and Technology* 6, 3 (2025), 035031.
- [20] François Rozet, Ruben Ohana, Michael McCabe, Gilles Louppe, François Lanusse, and Shirley Ho. 2025. Lost in Latent Space: An Empirical Study of Latent Diffusion Models for Physics Emulation. arXiv:2507.02608 [cs]
- [21] Hamees Sayed, Pranath Reddy, Michael W. Toomey, and Sergei Gleyzer. 2025. FlowLensing: Simulating Gravitational Lensing with Flow Matching. arXiv:2510.07878 [astro-ph]
- [22] Christopher J Shallue and Daniel J Eisenstein. 2023. Reconstructing Cosmological Initial Conditions from Late-Time Structure with Convolutional Neural Networks. *Monthly Notices of the Royal Astronomical Society* 520, 4 (April 2023), 6256–6267. doi:10.1093/mnras/stad528
- [23] Luigi Sigillo, Shengfeng He, and Danilo Comminiello. 2025. Latent Wavelet Diffusion: Enabling 4K Image Synthesis for Free. arXiv:2506.00433 [cs]
- [24] Yang Song and Stefano Ermon. 2020. Improved Techniques for Training Score-Based Generative Models. In *Advances in Neural Information Processing Systems*, Vol. 33. Curran Associates, Inc., Vancouver, Canada, 12438–12448.
- [25] Matthew Tancik, Pratul Srinivasan, Ben Mildenhall, Sara Fridovich-Keil, Nitin Raghavan, Utkarsh Singh, Ravi Ramamoorthi, Jonathan Barron, and Ren Ng. 2020. Fourier Features Let Networks Learn High Frequency Functions in Low Dimensional Domains. In *Advances in Neural Information Processing Systems*, Vol. 33. Curran Associates, Inc., Vancouver, BC, Canada, 7537–7547.
- [26] Georgios Valogiannis, Francisco Villaescusa-Navarro, and Marco Baldi. 2024. Towards unveiling the large-scale nature of gravity with the wavelet scattering transform. *Journal of Cosmology and Astroparticle Physics* 2024, 11 (2024), 061.
- [27] Francisco Villaescusa-Navarro. 2018. Pylians: Python libraries for the analysis of numerical simulations. *Astrophysics Source Code Library*, record ascl:1811.008, ascl:1811.008 pages. ascl:1811.008
- [28] Francisco Villaescusa-Navarro, ChangHoon Hahn, Elena Massara, Arka Banerjee, Ana Maria Delgado, Doogesh Kodi Ramanah, Tom Charnock, Elena Giusarma, Yin Li, Erwan Ally, Antoine Brochard, Cora Uhlemann, Chi-Ting Chiang, Siyu He, Alice Pisani, Andrej Obuljen, Yu Feng, Emanuele Castorina, Gabriella Contardo, Christina D. Kreisch, Andrina Nicola, Justin Alsing, Roman Scoccimarro, Licia Verde, Matteo Viel, Shirley Ho, Stephane Mallat, Benjamin Wandelt, and David N. Spergel. 2020. The Quijote Simulations. *The Astrophysical Journal Supplement Series* 250, 1 (Aug. 2020), 2. doi:10.3847/1538-4365/ab9d82
- [29] Simon D. M. White and Carlos S. Frenk. 1991. Galaxy Formation through Hierarchical Clustering. *The Astrophysical Journal* 379 (Sept. 1991), 52. doi:10.1086/170483
- [30] Maksim Zhdanov, Max Welling, and Jan-Willem van de Meent. 2025. Erwin: A Tree-based Hierarchical Transformer for Large-scale Physical Systems. arXiv:2502.17019 [cs]

A Appendix

Table 5 summarizes the notation and key definitions used throughout this paper.

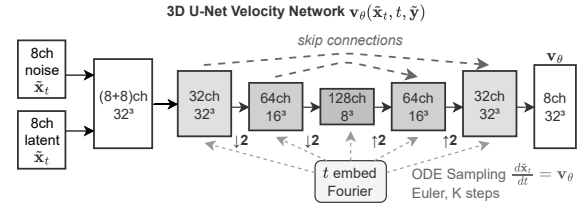


Figure 7: 3D U-Net Velocity Network Architecture for resolution 64. The velocity network takes concatenated noisy wavelet coefficients and conditioning observations (16 input channels) and predicts the velocity field in wavelet space (8 output channels). The encoder path consists of 2, 3, and 4 down/upsampling layers for image resolution 32, 64, and 128, respectively. This gains a common latent dimension of $8 \times 8 \times 8$. Each contains residual blocks with time embedding injection. The decoder mirrors the encoder with skip connections, enabling multi-scale feature propagation. The scale conditioning and cross-scale residuals is omitted for brevity, but explained in detailed at Algorithm 3.

A.1 3D U-Net Architecture Details

Figure 7 illustrates the detailed architecture of our 3D U-Net velocity network. The network follows an encoder-decoder structure specifically designed for volumetric cosmological data processing in wavelet space. We provide more details in Algorithm 3.

Input Processing. The network receives a 16-channel input by concatenating the noisy wavelet coefficients $\tilde{x}_t \in \mathbb{R}^{8 \times D/2 \times H/2 \times W/2}$

Table 5: Notation and key definitions used throughout this paper.

Symbol	Definition
<i>Problem Setup</i>	
$\mathbf{x} \in \mathbb{R}^{N^3}$	Initial conditions (latent state at $z = 127$)
$\mathbf{y} \in \mathbb{R}^{N^3}$	Observations (evolved state at $z = 0$)
N	Grid resolution per dimension (e.g., 128)
$p(\mathbf{x} \mathbf{y})$	Posterior distribution of initial conditions
$\delta = \rho/\bar{\rho} - 1$	Density contrast field
<i>Flow Matching</i>	
$t \in [0, 1]$	Flow time parameter
$\mathbf{x}_0 \sim p_0$	Sample from prior (Gaussian noise)
$\mathbf{x}_1 \sim p_1$	Sample from target data distribution
\mathbf{x}_t	Interpolated state: $t\mathbf{x}_1 + (1-t)\mathbf{x}_0$
\mathbf{u}_t	Target velocity field: $\mathbf{x}_1 - \mathbf{x}_0$
\mathbf{v}_θ	Learned velocity network (parameterized by θ)
K	Number of ODE integration steps
<i>Wavelet Transform</i>	
DWT / IDWT	Discrete Wavelet Transform / Inverse DWT
$\tilde{\mathbf{x}}, \tilde{\mathbf{y}}$	Wavelet-transformed fields
\mathbf{c}_{LL}	Approximation coefficients (low-frequency)
$\mathbf{c}_{LH}, \dots, \mathbf{c}_{HHH}$	Detail coefficients (7 high-frequency bands)
L, H	Low-pass and high-pass wavelet filters
<i>Training Objectives</i>	
\mathcal{L}_{FM}	Flow matching loss (pixel space)
\mathcal{L}_{flow}	Wavelet-space flow matching loss
\mathcal{L}_{PS}	Power spectrum regularization loss
λ_{PS}	Weight for power spectrum loss
<i>Evaluation Metrics</i>	
VRMSE	Variance-normalized root mean squared error
$P(k)$	Isotropic power spectrum at wavenumber k
$C(k)$	Cross-correlation coefficient at wavenumber k
$T(k)$	Transfer function: $\sqrt{P_{\text{pred}}(k)/P_{\text{true}}(k)}$

with the conditioning observation $\tilde{\mathbf{y}} \in \mathbb{R}^{8 \times D/2 \times H/2 \times W/2}$. An initial $3 \times 3 \times 3$ convolution projects this to the base feature dimension $n_f = 32$.

Encoder Structure. The encoder consists of 2, 3, and 4 down or upsampling layers for the image resolutions 32, 64, and 128, respectively. Each level contains $N_{\text{res}} = 2$ residual blocks that incorporate time conditioning through additive feature modulation. Spatial downsampling between levels is performed via strided average pooling with a factor of 2.

Bottleneck. At the coarsest resolution, the network processes features at 1/8 of the original spatial dimensions with 256 channels, capturing global context essential for coherent large-scale structure generation.

Algorithm 3 UNet Forward Pass with Scale Conditioning and Cross-Scale Skips

```

Require: Input  $\mathbf{w}_t$  (8 channels), time  $t$ , observations  $\tilde{\mathbf{y}}$  (8 channels)
Require: UNet with  $L$  resolution levels,  $N_{\text{res}}$  residual blocks per level
Ensure: Predicted velocity  $\mathbf{v}_t$ 

1:  $\mathbf{x} \leftarrow [\mathbf{w}_t; \tilde{\mathbf{y}}] \text{ // Concatenate: 16 channels}$ 
2:  $t_{\text{emb}} \leftarrow \text{GaussianFourierProjection}(t)$ 
3:  $t_{\text{emb}} \leftarrow \text{MLP}(t_{\text{emb}}) \text{ // Map to conditioning dimension}$ 
4: // Downsampling Path
5:  $\mathbf{h} \leftarrow \text{Conv}_{3 \times 3}(\mathbf{x}) \text{ // Initial convolution}$ 
6: Initialize skip connection list:  $\text{skips} \leftarrow [\mathbf{h}]$ 
7: Initialize cross-scale feature storage:  $\{\mathbf{s}_i\}$ 
8: for resolution level  $i = 0$  to  $L - 1$  do
9:   // Scale-Specific Conditioning Preparation
10:   $\mathbf{z}_i \leftarrow \text{Conv}_{1 \times 1}(\tilde{\mathbf{y}}) \text{ // Project 8 bands} \rightarrow C_i \text{ channels}$ 
11:  if  $i > 0$ :  $\mathbf{z}_i \leftarrow \text{AvgPool}_{2^i}(\mathbf{z}_i) \text{ // Match resolution}$ 
12:  for residual block  $j = 1$  to  $N_{\text{res}}$  do
13:     $\mathbf{h} \leftarrow \text{ResNetBlock}(\mathbf{h}, t_{\text{emb}}) \text{ // Standard residual block}$ 
14:    // Inject scale features
15:     $\mathbf{h} \leftarrow \mathbf{h} + \text{AdaptivePool}(\mathbf{z}_i, \mathbf{h}.shape)$ 
16:    Append  $\mathbf{h}$  to skips
17:  end for
18:  if  $i < L - 1$  then
19:     $\mathbf{h} \leftarrow \text{ResNetBlock}_{\text{down}}(\mathbf{h}, t_{\text{emb}}) \text{ // Downsample via stride-2}$ 
20:    Append  $\mathbf{h}$  to skips
21:  end if
22:   $\mathbf{s}_i \leftarrow \mathbf{h}.clone() \text{ // Store for cross-scale skip}$ 
23: end for
24: // Bottleneck Layer
25:  $\mathbf{h} \leftarrow \text{ResNetBlock}(\mathbf{h}, t_{\text{emb}}) \text{ // Middle block}$ 
26: // Upsampling Path
27: for resolution level  $i = L - 1$  down to 0 do
28:   for residual block  $j = 1$  to  $N_{\text{res}} + 1$  do
29:      $\mathbf{h}_{\text{skip}} \leftarrow \text{pop}(\text{skips}) \text{ // Standard U-Net skip}$ 
30:      $\mathbf{h} \leftarrow \text{ResNetBlock}([\mathbf{h}; \mathbf{h}_{\text{skip}}], t_{\text{emb}}) \text{ // Concatenate & process}$ 
31:   end for
32:   // Cross-Scale Residual Connection
33:   if  $\mathbf{s}_i.shape = \mathbf{h}.shape$ :
34:      $\mathbf{h} \leftarrow \mathbf{h} + \text{Conv}_{1 \times 1}(\mathbf{s}_i) \text{ // Add cross-scale features}$ 
35:   if  $i > 0$  then
36:      $\mathbf{h} \leftarrow \text{ResNetBlock}_{\text{up}}(\mathbf{h}, t_{\text{emb}}) \text{ // Upsample via transposed conv}$ 
37:   end if
38: assert  $\text{skips}$  is empty // Verify all skips consumed
39: // ===== Output =====
40:  $\mathbf{h} \leftarrow \text{Activation}(\text{GroupNorm}(\mathbf{h}))$ 
41:  $\mathbf{v}_t \leftarrow \text{Conv}_{3 \times 3}(\mathbf{h}) \text{ // Project to 8 output channels}$ 
42: return  $\mathbf{v}_t$ 

```

Decoder Structure. The decoder symmetrically mirrors the encoder, with each level receiving skip connections from the corresponding encoder stage. Features are upsampled via nearest-neighbor interpolation followed by convolution, then concatenated with skip features before processing through residual blocks. This design preserves fine-grained spatial information while incorporating global context.

Time Conditioning. The continuous time variable $t \in [0, 1]$ is embedded using Gaussian Fourier features with learnable frequencies, then projected through two dense layers with SiLU activations. The resulting embedding $\mathbf{e}_t \in \mathbb{R}^{128}$ is injected into each residual block via a dense projection added to the intermediate features.